Permeability anisotropy and its relations with porous medium structure

Jean-Baptiste Clavaud, Alexis Maineult, Maria Zamora, Patrick Rasolofosaon,
Camille Schlitter

HAL Id: insu-03603737
https://insu.hal.science/insu-03603737

Permeability anisotropy and its relations with porous medium structure

Jean-Baptiste Clavaud,[1,2] Alexis Maineult,[1] Maria Zamora,[1] Patrick Rasolofosaon,[3] and Camille Schlitter[3]

[1] The complete permeability tensor of 18 porous rock cores was determined by means of X-ray tomography monitoring during the displacement of a salty tracer. To study the effect of the pore space geometry on the anisotropy of permeability, we compared the three-dimensional shape of the invasion front with the X-ray porosity maps obtained before injection. The samples (clean and shale-bearing sandstones, limestones, and volcanic rocks) belong to a broad variety of granulometry and pore space geometry. Their porosity ranges from 12 to 57%, and their permeability ranges from 1.5×10^{-14} to 4×10^{-12} m^2. For sandstones the permeability anisotropy is well correlated with the presence of bedding. For volcanic rocks it is clearly related to the orientation of vesicles or cracks. However, for limestones, no evident link between the geometry of the porous network and the permeability anisotropy appears, probably because of the influence of the nonconnected porosity that does not contribute to the hydraulic transport. This systematic work evidences the ability and the limitations of the tracer method to characterize the anisotropy of permeability in the laboratory in a simple and rapid way.

1. Introduction

[2] Understanding the links between the topology of a porous medium and the anisotropic behavior of its transport properties is a crucial issue in many domains. One can mention production and recovery of hydrocarbons [e.g., *Selley*, 1985; *Chierici*, 1995; *King*, 1995; *Hanssen et al.*, 1995], water resource management and prediction of contaminant front advance [e.g., *Bear and Berkowitz*, 1987; *Zlotnik*, 1997; *Maréchal et al.*, 2003], pressure field and fluid flow in faulted zones [e.g., *Zhang et al.*, 1996; *Chen et al.*, 1999; *Zhang et al.*, 2001; *Nakaya et al.*, 2002], accretionary prisms [e.g., *Arch and Maltman*, 1990], oceanic crust [e.g., *Rosenberg et al.*, 1993], and hydrothermal areas [e.g., *Aron et al.*, 1996; *Wohletz and Heiken*, 1992]. Anisotropy is a vectorial variation of a physical property (such as elasticity, magnetization, or permeability) at one point, whereas heterogeneity is related to the intrinsic structure of the medium, in particular, to the composition and topology, and can be seen as a variation of a physical parameter (such as porosity or density) in space. Heterogeneity often causes anisotropy but is not a necessary condition. Moreover, at a scale larger than the length of heterogeneity a rock can appear homogeneous and anisotropic. The concepts of heterogeneity and anisotropy thus demand that the scale at which they are considered be precisely defined [e.g., *Dagan*, 1986; *Bernabé*, 1992].

[3] Heterogeneity and anisotropy of rocks strongly influence the way underground fluids propagate. Experimental, theoretical, and numerical studies focusing on the causes of the hydraulic anisotropy have therefore been carried out. The major features involved at small scale are the orientation of both the mineral grains and the pores [*Wright et al.*, 2006] or cracks [e.g., *Chen et al.*, 1999; *Popp et al.*, 2001; *Guéguen and Schubnel*, 2003] along a preferential direction, resulting directly from the formation of the rock or from the stress fields applied to it later [*Zoback and Byerlee*, 1976]. Bedding, foliation, shear, and compaction banding can also constitute barriers to flow, or at least reduce it [*Bruno*, 1994; *Zhu et al.*, 1997; *Olsson et al.*, 2002; *Holcomb and Olsson*, 2003; *Ngwenya et al.*, 2003; *Vajdova et al.*, 2004]. Dissolution and precipitation processes often increase the heterogeneity and the anisotropy while decreasing the connectivity [*Bernabé*, 1996; *Mok et al.*, 2002; *Ojala et al.*, 2004]. Heterogeneity and anisotropy can result in channeling of flow paths and even in retardation of mixing [e.g., *Bernabé and Bruderer*, 1998; *Bruderer-Weng et al.*, 2004; *Johnson et al.*, 2006]. At field scale, stratification in layers more or less permeable [e.g., *Chandler et al.*, 1989], clayey minerals in shear zones inducing alignment of grains [*Arch and Maltman*, 1990; *Faulkner and Rutter*, 1998; *Zhang and Tullis*, 1998; *Zhang et al.*, 2001; *Takahashi*, 2003], and preferential alignment of fractures and faults

---

[1]Equipe Géomatériaux et Environnement, Institut de Physique du Globe de Paris, Centre National de la Recherche Scientifique and Université Paris-Diderot, Paris, France.
[2]Now at Chevron Energy Technology Company, Houston, Texas, USA.
[3]Institut Français du Pétrole, Rueil Malmaison, France.

[*Zhang et al.*, 1996; *Nakaya et al.*, 2002; *Min et al.*, 2004] are sources of regional anisotropy.

[4] Over the last decades, elastic anisotropy has been abundantly documented because of its importance for seismics, seismology, and global dynamics [e.g., *Crampin*, 1981, 1984; *Thomsen*, 1986; *Pyrak-Nolte et al.*, 1990; *Arts*, 1993; *Silver*, 1996; *Weiss et al.*, 1999; *Rasolofosaon et al.*, 2000; *Tod and Liu*, 2002; *Guéguen and Schubnel*, 2003; *Louis et al.*, 2003, 2004; *Benson et al.*, 2003, 2005; *Baud et al.*, 2005; *Helbig and Thomsen*, 2005]. By contrast, only a few works have focused specifically on the theoretical and metrological aspects of the permeability anisotropy [*Scheidegger*, 1954, 1956; *Marcus*, 1962; *Bernabé*, 1992; *Bieber et al.*, 1996; *Renard et al.*, 2001].

[5] Neglecting the effects of the fluid and matrix compressibilities, and provided that the Reynolds number is low enough to ensure laminarity, the hydraulic flow through a porous medium is governed by Darcy's law:

$$\nabla \cdot \left(\frac{\overline{\overline{k}}}{\eta} \nabla P \right) = 0, \qquad (1)$$

where k is the permeability (in m^2), η is the fluid viscosity (in Pa s), and P is the hydraulic pressure (in Pa). The permeability tensor is of second-order and symmetric [*Scheidegger*, 1954, 1956; *Marcus*, 1962]. Hence the determination of the complete permeability tensor (i.e., its six components) requires only three measurements if the three main directions are known, six otherwise. The experimental difficulties encountered when measuring the permeability of a rock sample along different directions have constituted a major obstacle to systematic studies. Indeed, the methods available to estimate the permeability tensor are not numerous (for a review, see *Bernabé* [1992] and *Dullien* [1992]). Until recently, there have been two main ways to proceed directly. The tensor is reconstructed (1) from the permeability of different samples cored in a single block along different directions [e.g., *Scheidegger*, 1956; *Marcus*, 1962; *Faulkner and Rutter*, 1998] or (2) from the apparent permeability measured on a single sample along different directions [e.g., *Renard et al.*, 2001; *Louis et al.*, 2005]. However, these methods have several drawbacks. In particular, the measurements are time consuming, and the effects of the anisotropy cannot be easily separated from those of boundary conditions or rock's heterogeneities [*Bernabé*, 1992]. Indirect methods were also proposed, for which the topology of the pore space is determined experimentally in a first stage, for example, from microscopy, and the permeability is estimated numerically in a second stage [e.g., *O'Connor and Fredrich*, 1999; *Fredrich et al.*, 2006]. The analysis of the magnetic pore fabric described by *Pfleiderer and Halls* [1990, 1993, 1994] has some success [e.g., *Benson et al.*, 2003, 2005; *Louis et al.*, 2003, 2005; *Jones et al.*, 2006] in estimating the main directions of anisotropy. However, despite the quickness of its implementation, some difficulties still remain. First, the method averages the pore shape and size distributions over the sample and therefore is not accurate for highly heterogeneous rocks. Second, under the assumption of similarity between the anisotropy of the pore fabric and the anisotropy of permeability, it gives access to the three

eigendirections of the permeability tensor but not to the off-diagonal components. Finally, it does not provide any information on the absolute value of the permeability along the principal direction. Some authors also estimated the permeability of fractured rocks numerically from crack density functions deduced from velocity measurements in multiple directions but without satisfactorily recovering the absolute value of the permeability [e.g., *Gibson and Toksöz*, 1990].

[6] *Bieber et al.* [1996] and *Zhan and Yortsos* [2000] have suggested that the permeability tensor be estimated from the shape of a tracer front moving through rock samples. The displacement of the tracing fluid front is monitored in space and time using the X-ray tomography technique, a powerful tool for imaging the structure of porous media with a high resolution [e.g., *Lindquist et al.*, 2000; *Renard et al.*, 2004; *Monsen and Johnstad*, 2005; *Wright et al.*, 2006; *Goldstein et al.*, 2007]. Data inversion then provides the complete permeability tensor, coupled with its deviation from higher symmetries (i.e., isotropy). The technique is rapid and allows the results to be compared with porosity maps also obtained by the X-ray tomography before the injection, thus evidencing the correlations between the permeability anisotropy and the geometry of the porous structure. The experimental setup and methodology devised and validated by *Bieber et al.* [1996] were used successfully by *Rasolofosaon and Zinszner* [2002] to compare the permeability and elasticity tensors of some reservoir rocks. Here we used them on 18 samples representative of various types of rocks (clay-free and clayey sandstones, limestones, and volcanic rocks) to study the possible relations between the anisotropy of permeability and the porous structure.

2. Materials and Method

2.1. Samples

[7] In order to cover a wide range of both porosity and permeability, as well as to investigate the effects of various pore structures, we studied sandstones (samples hereinafter denoted FS, RS, RVS, and XS), limestones (SML, SPL, EspL, EstL, and BL) and volcanic rocks (MPP and VA). Their lithological characteristics are detailed in Table 1. The granulometry of the sandstones is fine (i.e., a few hundred micrometers) to coarse, and XS samples are clay/silt bearing. The grain size of the limestone samples ranges from 100 to 1000 μm, and they all contain bioclasts (algae, bryozoa, foraminifera, or oolites). Note that for sandstones and limestones a simple visual inspection did not reveal any heterogeneity. Concerning the volcanic rocks, the Volvic andesite (VA) exhibits a vuggy porosity with elongated, 0.1- to 2-mm-sized vesicles. The andesitic pumice from Mount Pelée (MPP) is microcracked and macrocracked.

[8] The length of the cylindrical cores ranged between 5.5 and 18.2 cm, and their diameter ranged between 5.9 and 8 cm (Table 1). The axes of the samples were either along the vertical geological axis z (or subperpendicular to the stratification when the exact z direction was unknown, V in Table 1) or along the geological horizontal direction x-y (or subparallel to the stratification, H in Table 1). We also measured the bulk porosity and permeability on cylindrical samples (2.5 cm in diameter and length) taken from the

Table 1. Samples' Lithology, Dimensions, and Orientation of the Cylinder's Axis[a]

Sample	Lithology	Length, cm	Diameter, cm	Orientation
FS	Fontainebleau sandstone/very pure, fine-grained, homogeneous	12.0	8.00	V
RS1	sandstone/fine-grained, bedding	6.20	5.96	H
RS2	sandstone/fine-grained, large bedding	8.10	6.00	V
RS3	sandstone/medium-grained, not bedded	5.60	5.95	H
RS4	sandstone/coarse-grained, no visible bedding	5.74	5.92	H
RS5	sandstone/coarse-grained, no visible bedding	6.20	5.96	H
RVS	Red Vosges sandstone/very fine grained, numerous large, silty and clayey bedding	5.74	7.19	V
XS1	sandstone/fine-grained, kaolinic, marked fine bedding	ND	ND	H
XS2	sandstone/medium-grained, kaolinic, marked fine bedding	ND	ND	H
XS3	sandstone/medium-grained, kaolinic, marked fine bedding	ND	ND	H
XS4	sandstone/coarse-grained, kaolinic, rare bedding	ND	ND	V
SML	Saint Maximin limestone/bioclastic, foraminiferous, important intergranular and intragranular macroporosity	7.61	7.94	V
SPL	Saint Pantaléon limestone/0.3- to 3-mm grains (badly sorted), some big bioclasts (1 cm), important intergranular macroporosity, microporosity in algae, some traces of silicification	18.2	7.70	H
EspL	Espeil limestone/0.5 mm to a few millimeters grains, bioclastic (algae, bryozoa), intergranular macroporosity (in bryozoa), important microporosity in algae	16.9	7.95	H
EstL	Estaillades limestone/0.5- to 1-mm grains (regular granulometry), bioclastic (algae), important intergranular macroporosity sometimes obstructed by calcite microcrystals, important microporosity in the bioclasts	10.4	8.00	H
BL	Brétigny limestone/>1-mm grains, oolitic, sparitic cement, intergranular macroporosity unequally distributed, intraoolitic microporosity	16.9	8.00	H
VA	Volvic andesite/glassy texture, rich in elongated feldspar phenocrystals (0.1 to 0.2 mm), vuggy porosity (elongated vesicles, 0.1 to 2 mm)	13.0	6.91	H
MPP	Mount Pelée pumice/andesitic, vuggy structure, microcracks and macrocracks	5.52	5.93	ND

[a]V indicates that the axis of the cylinder (Z axis, see Figure 1) is along the vertical direction, or subvertical (in a geological sense); H indicates that it is along the horizontal direction, or subhorizontal. ND, not determined.

original cores previously used for the miscible displacements experiments, along their main axis of permeability. The bulk connected porosity was determined by the triple weighting method once the samples were saturated under vacuum with degassed water. The air permeability was measured using *Bourbié and Zinszner*'s [1985] falling head permeameter, whose accuracy is within 1% for permeabilities greater than 10^{-16} m^2.
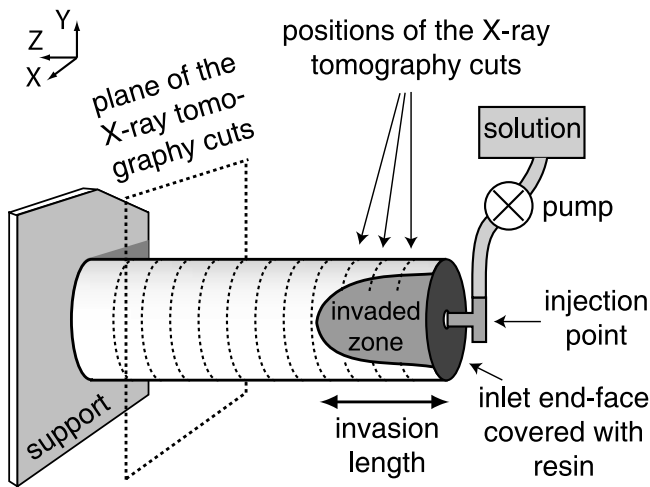
2.2. Experimental Procedures

2.2.1. Principle

[9] Let us consider a homogeneous, porous, and infinite medium, fully saturated with an incompressible fluid. If at a given source point S another perfectly miscible fluid with the same density is injected, then the invasion front (i.e., the interface between the two fluids) forms a surface so that the distance from any of its points M to S is proportional to the square root of the permeability along the considered direction MS [*Marcus*, 1962]. Therefore the invasion fronts are spherical in isotropic media and ellipsoidal in anisotropic ones. This also applies to a semi-infinite medium limited by a nonpermeable plane containing the injection point [*Bieber et al.*, 1996]. Thus the shape of the permeability tensor can be inferred from the characteristics of the

ellipsoids observed on laboratory cylinder-shaped samples in order to make their preparation and the data acquisition easier. The full permeability tensor can thus be inferred from the combination of the shape of the invaded zone with a single value of permeability measured along a known direction (for more details concerning the principle and the experimental procedures briefly summarized in sections 2.2.2, 2.2.3, and 2.2.4, see *Bieber et al.* [1996] and *Rasolofosaon and Zinszner* [2002]).

2.2.2. Experimental Device

[10] Figure 1 shows the experimental device schematically. Each cylindrical rock sample is fixed to a support allowing it to be positioned precisely in the X-ray scanner (General Electric scanner CE12000). The upstream end face is connected to a hydraulic circuit and made waterproof with epoxy resin around the injection point. The internal diameter of the injection pipe is 6 mm, so the injection surface represents less than 1% of the sample's section. The downstream face is glued to the support, and the lateral faces are free. A Cartesian reference frame is defined such as the Z axis corresponds to the direction of the cylindrical rock sample. The X-ray tomography cuts along the transverse direction (i.e., planes *X-Y*), having a virtual thickness of 1.5 and 5 mm spaced, are acquired successively. The

Figure 1. Scheme of the experimental device. The upstream end face of the sample is connected to a hydraulic circuit for tracer injection and glued with epoxy resin around the injection point. The X-ray tomography procedure samples the cylinder transversally, at various distances from the injection point (see text).

resolution of the scanner is such that one pixel corresponds to a surface of 0.2×0.2 mm^2.

2.2.3. Porosity Maps

[11] The sample is initially dry. After a first complete set of X-ray tomography cuts has been acquired, the sample is saturated with a primary fluid (potassium chloride solution at 25 g L^{-1}, except for the andesite, which is X-ray absorbent and for which barium chloride solution was used), and the tomography procedure is applied again. The difference between the second (fully saturated) and the first (dry) series of cuts provides maps of the porosity distribution. Each pixel presents a given grey tone resulting from the averaging of its void and rock contents. The intensity of the grey is then converted in terms of averaged porosity. So a map of the distribution of the bulk porosity at the resolution of 0.2×0.2 mm^2 is obtained. Note that hereinafter "porosity" will denote this "pixel-averaged" porosity, whereas "bulk porosity" will refer to the porosity measured on samples.

2.2.4. Tracer Experiment

[12] A small quantity of a secondary fluid (potassium iodide at 25 g L^{-1}) is injected in the KCl-saturated sample at low and constant flow rate to ensure a Darcian flow and no mechanical damage occurrence (10^{-3} to 10^{-2} mL s^{-1} depending on the permeability of the sample). The injected volume (comprised between 1 and 2 cm^3, depending on the porosity of the sample) is adjusted so that the tracer front is displaced from about 5 mm during the injection. Finally, the sample is imaged using X-ray tomography after the injection stopped. The injection and tomography procedures are then repeated until the front reaches the lateral or end face of the sample. Note that we used solutions of KCl and KI since they have a high radiological density contrast (KI is more X-ray absorbent) but the same specific mass, viscosity, and wettability and are thus perfectly miscible. During all the injection steps, performed at atmospheric pressure, the

fluid pressure at the injection point remained smaller than 400 mbar.

2.2.5. Determination of the Permeability Tensor

[13] The geometrical characterization of the interface between the primary and the secondary fluids requires some image processing, described briefly hereafter (see *Bieber et al.* [1996] and *Rasolofosaon and Zinszner* [2002] for more details). To remove the image component related to the solid matrix, from each image acquired during the injection phase we subtracted the corresponding image at the reference state (when the sample is saturated with KCl solution only). These "reduced" images, which contain information related to the distributions of KCl and KI solutions only, evidence the interface between the two fluids. The contour line (which corresponds to the 1-mm-thick contrast transition zone), delineating the invaded domain in the considered transverse section, is automatically detected by means of an isodensity method, based on constant density parameters for a given sample. It is then smoothed to eliminate high-frequency perturbations and to limit the number of points to a few hundred.

[14] For each injection step the three-dimensional shape of the invasion front is reconstructed from the whole set of contour lines at positions $Z_n = 5n$ mm, with $n = 0,\ldots,N$ so that $Z_N < L < 5(N + 1)$ mm, where L is the invasion length (i.e., the position of the top of the invaded zone along the Z axis, Figure 1). To homogenize the spatial distribution of the data, this reconstructed "raw" front is smoothed with a polynomial filter of the fifth degree; note that the choice of the fifth degree results from empirical trials performed by *Bieber et al.* [1996]. The final step consists in searching for the best ellipsoid that fits the smoothed experimental front, using a least squares method [*Arts*, 1993]. The normalized permeability tensor is then determined from the characteristics of this best fitting ellipsoid.

3. Results

3.1. Porosity Maps and Invasion Fronts

[15] The bulk porosity and permeability measured on 2.5 cm in diameter and length cores taken from the original samples (see section 2.1) are listed in Table 2. The bulk porosity is around 15% for the XS and Fontainebleau (FS) sandstones, 25% for the RS group, and equal to 20% for the red Vosges sandstone (RVS). The bulk connected porosity of the limestones ranges from 18 to 35% and is equal to 22% for the Volvic andesite and 57% for the Mount Pelée pumice. The permeability covers more than 2 orders of magnitude, from 1.5×10^{-14} to 4.1×10^{-12} m^2. There is no clear correlation between the permeability and the bulk porosity, even though for the sandstones the permeability tends to increase with the grain size and to decrease with the presence of bedding.

[16] The porosity maps obtained by X-ray tomography provide evidence regarding the heterogeneity of the samples. Concerning the sandstones, four of them are homogeneous (FS, RS3, RS4, and RS5), and the other is more or less heterogeneous, with bedding planes of very low porosity, ranging the thickness from a few millimeters (RS1, XS1, XS2, XS3) to 1 cm or more (RS2 and RVS). RS4 displays badly delineated zonations. Figures 2a and 2b show the porosity maps (determined following the procedure described

Table 2. Bulk Connected Porosity and Air Permeability[a]

Sample	Connected Porosity, %	Main Permeability, 10^{-15} m^2
FS	16.5	1050
RS1	24.0	30
RS2	23.0	90
RS3	24.5	1800
RS4	24.0	2200
RS5	25.0	1800
RVS	19.5	40
XS1	16.8	90
XS2	16.1	500
XS3	15.0	20
XS4	12.2	500
SML	26.2	1670
SPL	35.3	4070
EspL	28.5	1850
EstL	30.0	270
BL	17.8	15
VA	22.1	60
MPP	57.3	ND

[a]Measured on cylindrical samples (2.5 cm in diameter and length) cored along the main axis of permeability of the samples used for the miscible displacements experiments. ND, not determined.

in section 2.2.3) and the superimposed contour lines of the invasion front (determined following the procedure described in section 2.2.4) at various distances from the injection point for FS and XS2. Note that each color level of the porosity maps covers one tenth of the total surface (in other words, the color levels, with which given porosity ranges are associated, are equipopulated in terms of pixels). These samples constitute a summary of the two extreme behaviors that we observed in sandstones. FS's front is isotropic (note the quasi-circularity and the smoothness of the contour lines), even though the porosity distribution is somewhat heterogeneous but at a small scale. In contrast, XS2 is anisotropic, as a consequence of the bedding that can be distinguished very clearly in the porosity maps. The results for RS4 and RS5 are close to those obtained on FS. The porosity maps and invasion fronts of the others sandstones look similar to XS2 but to a less marked degree.

[17] The porosity of the limestones from Saint Maximin (SML, Figure 2c), Estaillades (EstL, Figure 2d), and Brétigny (BL, Figure 2f) appears to be heterogeneously distributed, with apparent correlation at a scale greater than the centimeter. In contrast, Saint Pantaléon (SPL, Figure 2e) and also Espeil limestones (not shown here, see Table 1) appear to be quite homogeneous, at least at the resolution of the X-ray tomography (i.e., pixels of 0.2×0.2 mm^2). Figures 2c–2f illustrate the complexity of hydraulic transport encountered in limestones: SPL (Figure 2e), even relatively homogeneous, is anisotropic (the contour of the front is ellipsoidal and indented); SML (Figure 2c), heterogeneous, is isotropic; EstL (Figure 2d) and BL (Figure 2f), heterogeneous, are anisotropic. The extremely tortuous shape of the invasion front for BL reflects the dramatic effect of the heterogeneity on the flow channeling.

[18] Figures 2g and 2h show the results for the volcanic samples. The Volvic andesite (Figure 2g) is strongly anisotropic with a preferential movement in the direction of the vesicles' elongation, even though it looks quite homogeneous (the contour line is rather smooth). The particular tracer displacement in the Mount Pelée pumice (Figure 2h) is explained by the presence of a main crack parallel to the axis of the sample.

3.2. Permeability Tensor, Deviation From Isotropy, and Anisotropy Ratio

[19] Table 3 gives the normalized eigenvalues $K_{\min}$, K_{int}, and $K_{\max}$ (such as $0 < K_{\min} < K_{\mathrm{int}} < K_{\max} = 1$), deduced from the diagonalization of the six-component permeability tensor expressed in the (X, Y, Z) reference frame associated with the samples (see *Arts* [1993] and *Bieber et al.* [1996] for the mathematical framework of the inversion in terms of permeability tensor). The invasion length L and the corresponding number of cuts used for the inversion procedure are listed in Table 3. Note that we used the images issued from the last invasion step before the front reached the external side of the core. The number of cuts considered in the inversion procedure was in any case greater than four (i.e., the invasion length was always greater than 15 mm). Nevertheless, the results of inversion for BL and MPP samples should be considered carefully. Indeed, the shape of the front is far from the ellipsoid, and therefore the inversion is poorly constrained.

[20] We define the degree of anisotropy by the quadratic deviation I of the permeability tensor from the "average" sphere of radius $K_{\mathrm{iso}} = (K_{\min} \, K_{\mathrm{int}} \, K_{\max})^{1/3}$, as

$$I = \left[\frac{(K_{\min} - K_{\mathrm{iso}})^2 + (K_{\mathrm{int}} - K_{\mathrm{iso}})^2 + (K_{\max} - K_{\mathrm{iso}})^2}{K_{\min}^2 + K_{\mathrm{int}}^2 + K_{\max}^2} \right]^{1/2}, \quad (2)$$

and we also define the anisotropy ratio R by

$$R = \frac{K_{\min}}{\sqrt{K_{\mathrm{int}} K_{\max}}}. \quad (3)$$

If the medium is transverse isotropic (i.e., the tensor defines a revolution ellipsoid) with the minimal value of the permeability along the geological vertical direction, R is equivalent to the classical ratio $r = k_V/k_H$, where k_V and k_H are the vertical and horizontal permeabilities, respectively (in a geological sense). However, if the stratification is dipping, the ratio r does not represent the actual anisotropy since the geological vertical axis does not correspond to the direction of the minimal permeability. That is the reason why we prefer to use R instead of r. To summarize, I represents a three-dimensional estimate of the deviation from isotropy, whereas R quantifies the transverse isotropy.

[21] For our samples the deviation from isotropy I is larger than 12% and rises up to 51% (Table 3). The anisotropy ratio R varies from 0.19 to 0.84; that is, the permeabilities along the axis of minimum permeability are 1.2 to 5 times smaller than the mean permeability in the perpendicular plane. Note that for the majority of samples the axis of $K_{\min}$ is close to the geological vertical direction. The cases for which a deviation from the vertical direction is observed correspond to the absence of bedding (such as for RS3 or RS4) or to a possible inclination of the bedding with respect to the horizontal geological direction.

4. Interpretation and Discussion

[22] The sandstone samples exhibit a wide range of behavior. Two of them are relatively close to isotropy, i.e., $I < 15\%$ and $R > 0.75$ (FS and RS4). Two are extremely anisotropic, i.e., $I > 40\%$ and $R < 0.3$ (RS1 and RVS).
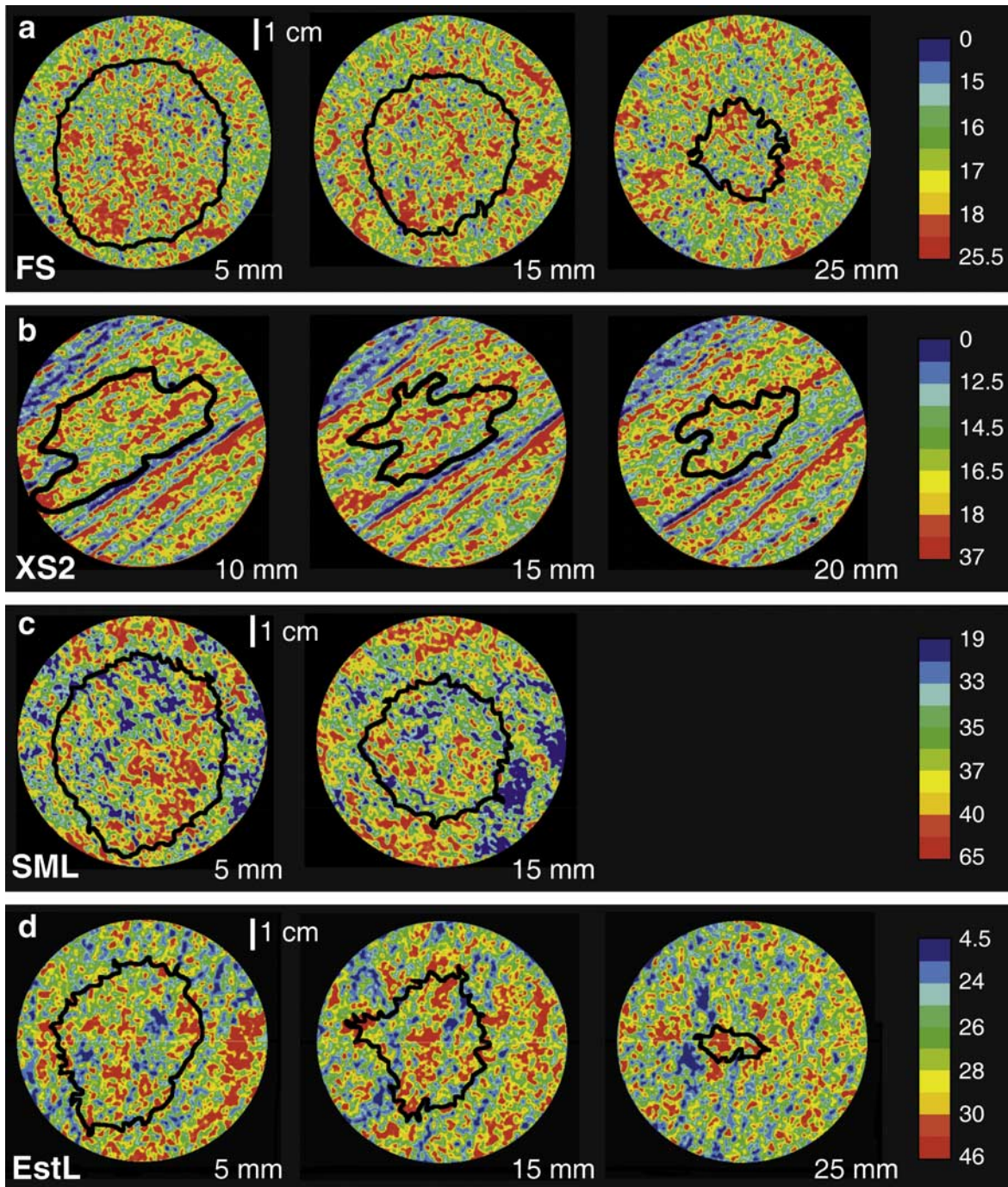
Figure 2. Porosity maps (determined following the procedure described in section 2.2.3.) and superimposed contour lines of the invasion front (determined following the procedure described in section 2.2.4.) at various distances for the sandstones (a) FS and (b) XS2, the limestones (c) SML, (d) EstL, (e) SPL, (f) BL, (g) the andesite VA, and (h) the pumice MPP. The total invasion length L was equal to 25 mm for XS2, SML, BL and VA; 30 mm for FS and EstL; 35 mm for SPL; and 40 mm for MPP. Note that each color bin of the porosity scale covers 10% of the total transversal area (see text).

However, the relation between the anisotropy of permeability and the geometry of the pore space is relatively simple, provided that two behaviors are distinguished:

[23] 1. Samples FS, RS4, and RS5 are roughly isotropic ($I < 25\%$). The permeability isotropy is certainly a consequence of the homogeneity of the pore space. For each

sample the contrast between the extreme values of the porosity on each cut is smaller than 25%. The porosity distribution is rather homogeneous: There is no apparent organization in its structure at the observation scale (porosity maps of RS4 and RS5, not shown here, are similar to those of FS displayed in Figure 2a). The anisotropy ratio,
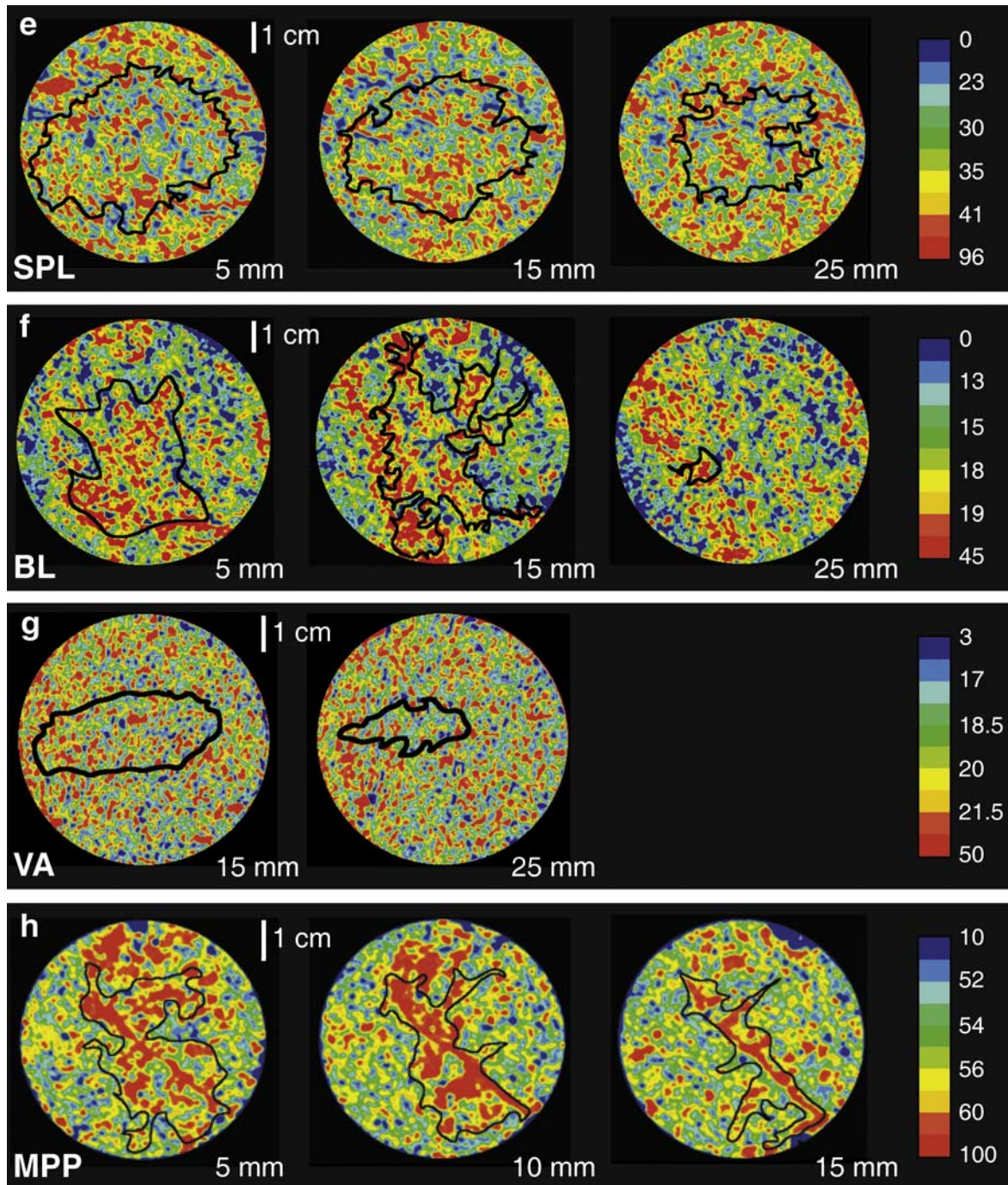
Figure 2. (continued)

between 0.65 (RS5) and 0.84 (RS4), is coherent with the value measured on unconsolidated sands by *Rice et al.* [1970], around 0.95, and on homogenous Vosges sandstone by *Bieber et al.* [1996], around 0.87. *Louis et al.* [2005] reported also a value between 0.67 and 0.81 on Bentheim sandstone, which is rather homogeneous at the centimetric scale.

[24] 2. All other sandstones are anisotropic. The anisotropy results from the planar beds of stratification with a low porosity, alternating with highly porous beds (Figure 2b). The horizontal permeability (in the direction parallel to the bedding plane) is controlled by the highly permeable sandy sediments. The vertical permeability (in the direction perpendicular to the bedding plane) is limited by the low permeability of the clay-rich silt beds, which act as barriers. This is similar, at laboratory scale, to what is observed at field scale in sedimentary reservoirs, where quasi- non-permeable beds induce strong anisotropy by preventing the fluids to flow along the direction perpendicular to the stratification [e.g., *Chandler et al.*, 1989]. The anisotropy ratio ranges from 0.19 (RVS) to 0.59 (XS3), with an average value around 0.4, consistent with the values obtained on

Table 3. Results[a]

Sample	L, mm/Cuts	K_X	K_Y	K_Z	K_{XY}	K_{XZ}	K_{YZ}	K_{max}	K_{int}	K_{min}	K_{min} Direction	I, %	R
FS	15/4	0.86	0.99	0.72	−0.04	0.005	0.03	1.00	0.85	0.71	V	14	0.77
RS1	15/4	0.91	0.36	0.78	−0.20	0.02	−0.15	1.00	0.80	0.26	V	43	0.29
RS2	20/5	0.98	0.95	0.44	−0.02	0.09	0.04	1.00	0.95	0.42	V	32	0.43
RS3	20/5	0.71	0.71	0.68	0.003	0.001	0.31	1.00	0.71	0.38	O	35	0.45
RS4	20/5	0.80	0.84	0.94	0.007	0.07	0.08	1.00	0.81	0.76	O	12	0.84
RS5	20/5	0.77	0.67	0.90	0.04	0.01	0.18	1.00	0.77	0.57	V	22	0.65
RVS	10/3	0.92	0.86	0.19	0.10	0.09	−0.08	1.00	0.80	0.17	V	51	0.19
XS1	15/4	0.98	0.61	0.49	0.02	0.10	−0.08	1.00	0.65	0.43	H	32	0.53
XS2	25/6	0.81	0.51	0.73	0.28	−0.03	−0.09	1.00	0.72	0.33	V	38	0.39
XS3	15/4	0.87	0.69	0.44	0.20	−0.02	0.02	1.00	0.56	0.44	H	34	0.59
XS4	20/5	0.70	0.79	0.66	−0.04	0.20	0.23	1.00	0.78	0.37	V	35	0.42
SML	20/5	0.87	0.95	0.67	−0.01	−0.03	0.12	1.00	0.87	0.62	V	19	0.66
SPL	25/6	0.61	0.37	0.99	−0.09	−0.06	0.04	1.00	0.63	0.34	V	39	0.43
EspL	20/5	0.93	0.65	0.66	0.10	−0.13	0.04	1.00	0.69	0.55	O	25	0.66
EstL	25/6	0.51	0.63	0.90	−0.06	−0.22	0.001	1.00	0.64	0.39	V	35	0.49
BL	15/4	*0.48*	*0.83*	*0.22*	*−0.20*	*−0.17*	*0.20*	*1.00*	*0.41*	*0.12*	H	*63*	*0.19*
VA	25/6	0.95	0.28	0.81	−0.13	−0.07	0.04	1.00	0.78	0.25	V	44	0.28
MPP	20/5	*0.30*	*0.86*	*0.59*	*0.27*	*−0.01*	*0.13*	*1.00*	*0.56*	*0.18*	ND	*53*	*0.24*

[a]Length of invasion L and corresponding number of cuts used for inversion, components of the normalized permeability tensor in the sample's frame (K_X, K_Y, K_Z, K_{XY}, K_{XZ}, and K_{YZ}), normalized eigenvalues of the tensor (K_{max}, K_{int}, and K_{min}), orientation of K_{min} (V, along the geological vertical direction; H, along the horizontal; O, along another direction), deviation to the isotropy I, and R ratio. ND, not determined. Italic values are poorly constrained (see text).

bedded sandstones, such as Crab Orchard sandstone (0.41 [*Benson et al.*, 2003]), Treves Sandstone (0.48 [*Bieber et al.*, 1996]), or Rothbach sandstone (0.2 [*Louis et al.*, 2005]).

[25] The anisotropic group can be divided into two subgroups. In the first one (XS1 to XS4, and RVS) the heterogeneity results from the presence of numerous very thin beds separated by a few millimeters (Figure 2b). The porosity of these beds is smaller than 10%, whereas the porosity surrounding material reaches about 35%. In this case, the observation scale (see Table 1) is much larger than the homogenization volume of the permeability, and the method is convenient to determine the permeability tensor. For the second subgroups (RS1 to RS3) the relationship between the permeability anisotropy and the porous structure is not so clear. Small low-porosity areas oriented along preferential directions are observed, but they do not form clearly delineated and continuous beds. However, this orientation brings on a well-pronounced anisotropy. Note, finally, that in the case of RS1 and RS2, as well as RVS, the permeability tensor is transverse isotropic, i.e., K_{int} is close to K_{max} ($K_{min}/K_{max} \geq 0.8$).

[26] In limestone and volcanic rock samples the pore space topology of which is more complicated, the relationship between the permeability anisotropy and the pore space geometry appears to be also more complex. The deviation from isotropy is greater on average than for sandstones and the anisotropy ratio smaller. Uncommon behaviors can be seen, such as the Saint Maximin sample (Figure 2c). Although its porosity map exhibits a strong heterogeneity, with low-porosity (less than 20%) areas alternating with extremely porous zones (up to 65%), the shape of the invasion front proves that the permeability tensor is relatively transverse isotropic (with a deviation of 19% and K_{int} close to K_{max}). Saint Pantaléon limestone's front is quite similar, but more indented, due to a more pronounced heterogeneity (Figure 2e). The samples from Estaillades (Figure 2d) and Brétigny (Figure 2f) present similar, X-ray determined porosity maps (in terms of spatial distribution), but they behave quite differently regarding the permeability anisotropy, as evidenced by the totally different shapes of

the invasion fronts. We suggest that the cause of this difference in behavior lies in the double-porosity network, and particularly in the connectivity and heterogeneity of the microporosity. Indeed, the microporous topology may vary from one type of limestone to the other because of the intrinsic constitution (particularly the type of bioclasts) and/or to diagenetic dissolution and cementation processes. For example, the low-porosity zones of EstL correspond to the deposits of algae, which do not contribute to the hydraulic transport, despite its relatively high microporosity. Unfortunately, the resolution of the X-ray scanner (0.2×0.2 mm^2) was not fine enough to characterize the intragranular and intraclastic porosity of the samples, the length scale of which ranges from 0.01 to 1 μm, to be compared with the $5-500$ μm range for macroporosity. So, although the method allowed us to quantify the permeability anisotropy and the heterogeneity of the macroporous space, devising a more refined relation between topological structure and transport properties will require some improvement in the scanner resolution. The anisotropy ratio lies between 0.4 and 0.66, except for Brétigny limestone (0.19, but this last value is poorly constrained because of the shape of the invasion front which is not ellipsoidal). These values are a little higher than reported elsewhere, i.e., between 0.03 and 0.3. *Rice et al.* [1970] reported values of 0.8 to 0.9 but on crushed samples. This discrepancy underlines the strong effect of the solid rock structure on the anisotropy.

[27] The very strong anisotropy of the Volvic andesite (Figure 2g) is a consequence of the flattening and the preferential orientation of the vesicles resulting from degassing and possibly from cooling under flowing conditions. Here the anisotropy is the result of the particular geometry of the rock. The minimum permeability is along the direction perpendicular to the plane of elongation, in accordance with the observations made by *Wright et al.* [2006] on four types of pumices. The explanation here is similar to the conceptual model devised by *Louis et al.* [2003, 2005] for the Bentheim sandstone, for which the anisotropy is due to the elongated shape of the pores along one preferential direction. However, once again the X-ray

scanning was not sufficiently precise to provide evidence relating to the porosity. The hydraulic behavior of the Mount Pelée pumice (Figure 2h) was controlled by a major crack clearly marked on the porosity maps, which drained the main part of the fluid. The sample size was, in this case, smaller than the homogenization length, and as a consequence, the results of the inversion are not valid.

5. Conclusions

[28] This study shows that for the considered sandstones the anisotropy of permeability is directly linked to the petrographic structure at the millimetric scale. A small value of the anisotropy ratio R (corresponding to a high anisotropy) correlates with the presence of silt beds, the horizontal permeability being controlled by the highly permeable clay-free layers and the vertical permeability being determined by the shale content of the less permeable silty layers. The main factor that induces the anisotropy is the presence of bedding. Concerning the limestones, the effect of the millimetric petrographic structure is not as evident, as some beds, clearly marked on the porosity maps, induce no strong anisotropy (such as for Estaillades limestone), while others do (such as for Brétigny limestone). The explanation for such different behaviors is likely to be related to the material properties at the micrometric scale, i.e., in the properties of the microporous network, which can contribute, or not, to the hydraulic transport. The development of more focused X-ray scanners, or at least the combination with other techniques such as microscopy, will be required to examine this issue closer. Finally, in the two representative samples of volcanic rocks which we have analyzed, the presence of cracks (as in pumice) or fluidal structures (such as oriented vesicles in andesite) is the main factor causing anisotropy.

[29] The method first described by *Bieber et al.* [1996] allows an overall characterization of the permeability anisotropy at the centimetric scale, coupled with an estimation of the porosity distribution. The experiments are performed in a simple and rapid manner, albeit limited by the availability of X-ray tomography instruments. The scale limitation is only linked to the device we used. Since this tracer method works rather well in the laboratory, one can expect to extend it at field scale (metric to decametric), thus offering practical applications in hydrogeophysics. Indeed, the monitoring of propagation of salty fronts in the subsurface can be performed using geophysical methods such as electrical tomography or ground-penetrating radar [e.g., *Kemna et al.*, 2002; *Sandberg et al.*, 2002; *Bauer et al.*, 2006]. An extension of the method into a field methodology would require some validation experiments at a greater scale in controlled conditions, in the laboratory as well as on test sites.

References

Arch, J., and A. Maltman (1990), Anisotropic permeability and tortuosity in deformed wet sediments, *J. Geophys. Res.*, 95, 9035–9045.

Aron, C., P. A. Pezard, P. Angot, and C. Laverne (1996), Hydrothermal convection at mid-ocean ridges: Influence of permeability anisotropy within a tilted triangular structure, *Geophys. Res. Lett.*, 23, 3127–3130.

Arts, R. J. (1993), A study of general anisotropic elasticity in rocks by wave propagation: Theoretical and experimental aspects, Ph.D. thesis, Univ. Pierre et Marie Curie, Paris.

Baud, P., L. Louis, C. David, G. R. Rawling, and T. F. Wong (2005), Effects of bedding and foliation on mechanical anisotropy, damage evolution and failure mode, in *High-Strain Zones: Structure and Physical Properties*, edited by D. Bruhn and L. Burlini, *Geol. Soc. Spec. Publ.*, 245, 223–249.

Bauer, P., R. Supper, S. Zimmermann, and W. Kinzelbach (2006), Geoelectrical imaging of groundwater salinization in the Okavango Delta, Botswana, *J. Appl. Geophys.*, 60, 126–141.

Bear, J., and B. Berkowitz (1987), Groundwater flow and pollution in fractured rock aquifers, in *Developments in Hydraulic Engineering*, edited by P. Novak, pp. 175–238, Elsevier, Amsterdam.

Benson, P. M., P. G. Meredith, and E. S. Platzman (2003), Relating pore fabric geometry to acoustic and permeability anisotropy in Crab Orchard sandstone: A laboratory study using magnetic ferrofluid, *Geophys. Res. Lett.*, 30(19), 1976, doi:10.1029/2003GL017929.

Benson, P. M., P. G. Meredith, E. S. Platzman, and R. E. White (2005), Pore fabric shape anisotropy in porous sandstones and its relation to elastic wave velocity and permeability anisotropy under hydrostatic pressure, *Int. J. Rock Mech. Min. Sci.*, 42, 890–899.

Bernabé, Y., (1992), On the measurements of permeability in anisotropic rocks, in *Fault Mechanics and Transport Properties of Rocks*, edited by B. Evans and T.-F. Wong, pp. 147–167, Academic, London.

Bernabé, Y. (1996), Self-organized fluid flow through heterogeneous network, *Geophys. Res. Lett.*, 23, 3039–3042.

Bernabé, Y., and C. Bruderer (1998), Effect of the variance of pore size distribution on the transport properties of heterogeneous networks, *J. Geophys. Res.*, 103, 513–525.

Bieber, M. T., P. Rasolofosaon, B. Zinszner, and M. Zamora (1996), Measurements and overall characterization of permeability anisotropy by tracer injection, *Rev. Inst. Fr. Pet.*, 51, 333–347.

Bourbié, T., and B. Zinszner (1985), Hydraulic and acoustic properties as a function of porosity in Fontainebleau sandstone, *J. Geophys. Res.*, 90, 11,524–11,532.

Bruderer-Weng, C., P. Cowie, Y. Bernabé, and I. Main (2004), Relating flow channeling to tracer dispersion in heterogeneous networks, *Adv. Water Resour.*, 27, 843–855.

Bruno, M. S. (1994), Micromechanics of stress-induced permeability anisotropy and damage in sedimentary rocks, *Mech. Mater.*, 18, 31–48.

Chandler, M. A., G. Kocurek, D. J. Coggin, and L. W. Lake (1989), Effects of stratigraphic heterogeneity on permeability in eolian sandstone sequence: Page sandstone, northern Arizona, *AAPG Bull.*, 73, 658–668.

Chen, M., M. Bai, and J.-C. Roegiers (1999), Permeability tensors of anisotropic fracture networks, *Math. Geol.*, 31, 355–373.

Chierici, G. L. (1995), *Principles of Petroleum Reservoir Engineering*, 430 pp., Springer, Berlin.

Crampin, S. (1981), A review of wave motion in anisotropic and cracked elastic-media, *Wave Motion*, 3, 343–391.

Crampin, S. (1984), An introduction to wave propagation in anisotropic media, *Geophys. J. R. Astron. Soc.*, 76, 135–145.

Dagan, G. (1986), Statistical theory of groundwater flow and transport: Pore to laboratory, laboratory to formation, and formation to regional scale, *Water Resour. Res.*, 22, 120S–134S.

Dullien, F. A. L. (1992), *Porous Media: Fluid Transport and Pore Structure*, 2nd ed., 574 pp., Academic, New York.

Faulkner, D. R., and E. H. Rutter (1998), The gas permeability of clay-bearing fault gouge at 20°C, in *Faulting, Fault Sealing and Fluid Flow in Hydrocarbon Reservoirs*, edited by G. Jones, Q. J. Fisher, and R. J. Knipe, *Geol. Soc. Spec. Publ.*, 147, 147–156.

Fredrich, J. T., A. A. DiGiovanni, and D. R. Noble (2006), Predicting macroscopic transport properties using microscopic image data, *J. Geophys. Res.*, 111, B03201, doi:10.1029/2005JB003774.

Gibson, R. L., Jr., and M. N. Toksöz (1990), Permeability estimation from velocity anisotropy in fractured rock, *J. Geophys. Res.*, 95, 15,643–15,655.

Goldstein, L., S. O. Prasher, and S. Ghoshal (2007), Three-dimensional visualization and quantification of non-aqueous phase liquid volumes in natural porous media using a medical X-ray computed tomography scanner, *J. Contam. Hydrol.*, 93, 96–110.

Guéguen, Y., and A. Schubnel (2003), Elastic wave velocities and permeability of cracked rocks, *Tectonophysics*, 370, 163–176.

Hanssen, J. E., L. M. Surguchev, I. Svorstøl, and T. Blaker (1995), SAGA injection: A new combination IOR process for stratified reservoirs, in *New Developments in Improved Oil Recovery*, edited by H. J. De Haan, *Geol. Soc. Spec. Publ.*, 84, 111–123.

Helbig, K., and L. Thomsen (2005), 75-plus years of anisotropy in exploration and reservoir seismics: A historical review of concepts and methods, *Geophysics*, 70, 9ND–23ND, doi:10.1190/1.2122407.

Holcomb, D. J., and W. A. Olsson (2003), Compaction localization and fluid flow, *J. Geophys. Res.*, 108(B6), 2290, doi:10.1029/2001JB000813.

Johnson, J., S. Brown, and H. Stockman (2006), Fluid flow and mixing in rough-walled fracture intersections, *J. Geophys. Res.*, 111, B12206, doi:10.1029/2005JB004087.

Jones, S., P. Benson, and P. Meredith (2006), Pore fabric anisotropy: Testing the equivalent pore concept using magnetic measurements on synthetic voids of known geometry, *Geophys. J. Int.*, 166, 485–492.

Kemna, A., J. Vanderborght, B. Kulessa, and H. Vereecken (2002), Imaging and characterisation of subsurface solute transport using electrical resistivity tomography (ERT) and equivalent transport models, *J. Hydrol.*, 267, 125–146.

King, M. J. (1995), Application and analysis of a new method for calculating tensor permeability, in *New Developments in Improved Oil Recovery*, edited by H. J. De Haan, *Geol. Soc. Spec. Publ.*, 84, 19–27.

Lindquist, W. B., A. Venkatarangan, J. Dunsmuir, and T. Wong (2000), Pore and throat size distributions measured from synchrotron X-ray tomographic images of Fontainebleau sandstones, *J. Geophys. Res.*, 105, 21,509–21,527.

Louis, L., C. David, and P. Robion (2003), Comparison of the anisotropic behaviour of undeformed sandstones under dry and saturated conditions, *Tectonophysics*, 370, 193–212.

Louis, L., P. Robion, and C. David (2004), A single method for the inversion of anisotropic data sets with application to structural studies, *J. Struct. Geol.*, 26, 2065–2072.

Louis, L., C. David, V. Metz, P. Robion, B. Menéndez, and C. Kissel (2005), Microstructural control on the anisotropy of elastic and transport properties in undeformed sandstones, *Int. J. Rock Mech. Min. Sci.*, 42, 911–923.

Marcus, H. (1962), The permeability of a sample of an anisotropic porous medium, *J. Geophys. Res.*, 67, 5215–5225.

Maréchal, J.-C., R. Wyns, P. Lachassagne, K. Subrahmanyam, and F. Touchard (2003), Anisotropie verticale de la perméabilité de l'horizon fissuré des aquifères de socle: Concordance avec la structure géologique des profils d'altération, *C. R. Geosci.*, 335, 451–460.

Min, K.-B., J. Rutqvist, C.-F. Tsang, and L. Jing (2004), Stress-dependent permeability of fractured rock masses: A numerical study, *Int. J. Rock Mech. Min. Sci.*, 41, 1191–1210.

Mok, U., Y. Bernabé, and B. Evans (2002), Permeability, porosity and pore geometry of chemically altered porous silica glass, *J. Geophys. Res.*, 107(B1), 2015, doi:10.1029/2001JB000247.

Monsen, K., and S. E. Johnstad (2005), Improved understanding of velocity-saturation relationships using 4D computer-tomography acoustic measurements, *Geophys. Prospect.*, 53, 173–181.

Nakaya, S., T. Yohmei, A. Koike, T. Hirayama, T. Yoden, and M. Nishigaki (2002), Determination of anisotropy of spatial correlation structure in a three-dimensional permeability field accompanied by shallow faults, *Water Resour. Res.*, 38(8), 1160, doi:10.1029/2001WR000672.

Ngwenya, B. T., O. Kwon, S. C. Elphick, and I. G. Main (2003), Permeability evolution during progressive development of deformation bands in porous sandstones, *J. Geophys. Res.*, 108(B7), 2343, doi:10.1029/2002JB001854.

O'Connor, R. M., and J. T. Fredrich (1999), Microscale flow modelling in geological materials, *J. Phys. Chem. A*, 24, 611–616.

Ojala, I. O., B. T. Ngwenya, and I. G. Main (2004), Loading rate dependence of permeability evolution in porous aeolian sandstones, *J. Geophys. Res.*, 109, B01204, doi:10.1029/2002JB002347.

Olsson, W. A., D. J. Holcomb, and J. W. Rudnicki (2002), Compaction localization in porous sandstone: Implications for reservoir mechanics, *Oil Gas Sci. Technol.*, 57, 591–599.

Pfleiderer, S., and H. C. Halls (1990), Magnetic susceptibility anisotropy of rocks saturated with ferrofluid: A new method to study pore fabric?, *Phys. Earth Planet. Inter.*, 65, 158–164.

Pfleiderer, S., and H. C. Halls (1993), Magnetic pore fabric analysis: Verification through image autocorrelation, *J. Geophys. Res.*, 98, 4311–4316.

Pfleiderer, S., and H. C. Halls (1994), Magnetic pore fabric analysis: A rapid method for estimating permeability anisotropy, *Geophys. J. Int.*, 116, 39–45.

Popp, T., H. Kern, and O. Schulze (2001), Evolution of dilatancy and permeability in rock salt during hydrostatic compaction and triaxial deformation, *J. Geophys. Res.*, 106, 4061–4078.

Pyrak-Nolte, L. J., L. R. Myer, and N. G. W. Cook (1990), Anisotropy in seismic velocities and amplitudes from multiple parallel fractures, *J. Geophys. Res.*, 95, 11,345–11,358.

Rasolofosaon, P. N. J., and B. E. Zinszner (2002), Comparison between permeability anisotropy and elasticity anisotropy of reservoir rocks, *Geophysics*, 67, 230–240.

Rasolofosaon, P. N. J., W. Rabbel, S. Siegesmund, and A. Vollbrecht (2000), Characterization of crack distribution: Fabric analysis versus ultrasonic inversion, *Geophys. J. Int.*, 141, 413–424.

Renard, F., D. Bernard, X. Thibault, and E. Boller (2004), Synchrotron 3D microtomography of halite aggregates during experimental pressure solution creep and evolution of the permeability, *Geophys. Res. Lett.*, 31, L07607, doi:10.1029/2004GL019605.

Renard, P., A. Genty, and F. Stauffer (2001), Laboratory determination of the full permeability tensor, *J. Geophys. Res.*, 106, 26,443–26,452.

Rice, P. A., D. J. Fontugne, R. G. Latini, and A. J. Barduhn (1970), Anisotropic permeability in porous media, *Ind. Eng. Chem.*, 62, 23–31.

Rosenberg, N. D., F. J. Spera, and R. M. Haymon (1993), The relationship between flow and permeability field in seafloor hydrothermal systems, *Earth Planet. Sci. Lett.*, 116, 135–153.

Sandberg, S. K., L. D. Slater, and R. Versteeg (2002), An integrated geophysical investigation of the hydrogeology of an anisotropic unconfined aquifer, *J. Hydrol.*, 267, 227–243.

Scheidegger, A. E. (1954), Directional permeability of porous media to homogeneous fluids, *Geofis. Pura Appl.*, 28, 75–91.

Scheidegger, A. E. (1956), On directional permeability, *Geofis. Pura Appl.*, 33, 111–113.

Selley, R. C. (1985), *Elements of Petroleum Geology*, 449 pp., W. H. Freeman, New York.

Silver, P. G. (1996), Seismic anisotropy beneath the continents: Probing the depths of geology, *Annu. Rev. Earth Planet. Sci.*, 24, 385–432.

Takahashi, M. (2003), Permeability change during experimental fault smearing, *J. Geophys. Res.*, 108(B5), 2234, doi:10.1029/2002JB001984.

Thomsen, L. (1986), Weak elastic anisotropy, *Geophysics*, 51, 1954–1966.

Tod, S. R., and E. Liu (2002), Frequency-dependent anisotropy due to fluid flow in bed limited cracks, *Geophys. Res. Lett.*, 29(15), 1749, doi:10.1029/2002GL015369.

Vajdova, V., P. Baud, and T. Wong (2004), Permeability evolution during localized deformation in Bentheim sandstone, *J. Geophys. Res.*, 109, B10406, doi:10.1029/2003JB002942.

Weiss, T., S. Siegesmund, W. Rabbel, T. Bohlen, and M. Pohl (1999), Seismic velocity and anisotropy of the lower continental crust: A review, *Pure Appl. Geophys.*, 156, 97–122.

Wohletz, K., and G. Heiken (1992), *Volcanology and Geothermal Energy*, 432 pp., Univ. of Calif. Press, Berkeley.

Wright, H. M. N., J. J. Roberts, and K. V. Cashman (2006), Permeability of anisotropic tube pumice: Model calculations and measurements, *Geophys. Res. Lett.*, 33, L17316, doi:10.1029/2006GL027224.

Zhan, L., and Y. C. Yortsos (2000), Identification of the permeability field of a porous medium from the injection of a passive tracer, *Phys. Rev. E*, 62, 863–879.

Zhang, S., and T. E. Tullis (1998), The effect of fault slip on permeability and permeability anisotropy in quartz gouge, *Tectonophysics*, 295, 41–52.

Zhang, S., T. E. Tullis, and V. S. Scrugges (2001), Implications of permeability and its anisotropy in a mica gouge for pore pressures in fault zones, *Tectonophysics*, 335, 37–50.

Zhang, X., D. J. Sanderson, R. M. Harkness, and N. C. Last (1996), Evaluation of the 2-D permeability tensor for fractured rock masses, *Int. J. Rock Mech. Min. Sci.*, 33, 17–37.

Zhu, W., L. G. J. Montesi, and T.-F. Wong (1997), Shear-enhanced compaction and permeability reduction: Triaxial extension tests on porous sandstone, *Mech. Mater.*, 25, 199–214.

Zlotnik, V. A. (1997), Effects of anisotropy on the capture zone of a partial penetrating well, *Ground Water*, 35, 842–848.

Zoback, M. D., and J. D. Byerlee (1976), Effect of high-pressure deformation on permeability of Ottawa sand, *AAPG Bull.*, 60, 1531–1542.

————————————

J.-B. Clavaud, Chevron Energy Technology Company, 1500 Louisiana Street, Houston, TX 77002, USA.

A. Maineult and M. Zamora, Equipe Géomatériaux et Environnement, Institut de Physique du Globe de Paris, CNRS et Université Paris-Diderot, Tour 14, 4 place Jussieu, F-75005 Paris, France. (maineult@ipgp.fr)

P. Rasolofosaon and C. Schlitter, Institut Français du Pétrole, 1-4 avenue de Bois-Préau, F-92500 Rueil Malmaison, France.